Accepted Manuscript

Phase and microstructure formation in rapidly solidified Cu-Sn and Cu-Sn-Ti alloys

X. Li, T. Ivas, A.B. Spierings, K. Wegener, C. Leinenbach

Please cite this article as: X. Li, T. Ivas, A.B. Spierings, K. Wegener, C. Leinenbach, Phase and microstructure formation in rapidly solidified Cu-Sn and Cu-Sn-Ti alloys, *Journal of Alloys and Compounds* (2017), doi: 10.1016/j.jallcom.2017.11.237.

Phase and microstructure formation in rapidly solidified Cu-Sn and Cu-Sn-Ti alloys

X. Li[1,3], T. Ivas[1], A.B. Spierings[2], K. Wegener[3], C. Leinenbach[1,*]

1. Empa-Swiss Federal Laboratories for Materials Science and Technology, Überlandstrasse 129, 8600 Dübendorf, Switzerland

2. Innovation Center for Additive Manufacturing Switzerland, Inspire AG, Lerchenfeldstrasse 3, 9014 St. Gallen, Switzerland

3. Institute of Machine Tools and Manufacturing, ETH Zurich, Leonhardstrasse 21, Zurich, Switzerland

*) Corresponding author: christian.leinenbach@empa.ch, Tel: +41 58 765 4518

Abstract:

In this work, the microstructure and phase formation in binary Cu-Sn and ternary Cu-Sn-Ti alloys under rapid solidification conditions are studied as a function of alloy composition and cooling rate and compared to the results from solidification at low cooling rate in a Differential Scanning Calorimetry furnace. At high cooling rates (10^3 - 10^4 K/s) a metastable $Cu_{5.6}Sn$ phase is observed in all selected binary alloys, which could be explained to have formed via diffusionless martensitic transformation from the parent β phase. An increasing amount of Sn results in the transition of preferential phase formation in the sequence of α, $Cu_{5.6}Sn$ and δ. In the ternary alloys, Ti is observed to form $(Cu,Sn)_3Ti_5$ compound at both low and high cooling rates due to the low solubility of Ti in the α phase, and the fraction of $(Cu,Sn)_3Ti_5$ and α phases tend to increase with increasing Ti amount but that of $Cu_{5.6}Sn$ decreases. The results are of relevance for the development and optimization of Cu-Sn based alloys for processing techniques involving rapid solidification with varying cooling rates, e.g. laser additive manufacturing.

Keywords: rapid solidification; tin bronze; microstructure; phase transitions; thermodynamic modeling

1 Introduction

Selective Laser Melting (SLM) is a powder bed based additive manufacturing (AM) technique with which 3D parts are built up layer by layer, which opens the possibility to make parts even with intricate geometries. The technology is already widely used for manufacturing parts from e.g. stainless steel, Ni alloys or Ti alloys [1,2]. Cu-Sn (bronze) alloys are applied extensively in mechanical and electronic industries because of their outstanding properties, such as high strength and thermal conductivity, good wear resistances and good weldability, or as braze and solder alloys for joining technologies [3]. Over the last decade, attempts were also made to fabricate Cu-Sn based alloys by AM, e.g. tin bronze [4–6]. The rapid consolidation during AM allows for the processing of metastable material combinations like diamond with metal, and Cu-Sn and Cu-Sn-Ti alloys were successfully used as matrix material in metal-diamond composites [7,8], opening new possibilities for the design and fabrication of e.g. abrasive tools. However, the fabrication of defect-free samples from a commercial Cu-14.4Sn-10.2Ti-1.5Zr with acceptable mechanical properties was very challenging [8].

From the material science perspective, the SLM process can be considered as a sequence of rapid solidification (RS) of small material volumes followed by the cyclic heat treatment with high heating and cooling rates (10^2 - 10^6 K/s) during the deposition of succeeding layers [9]. These conditions may lead to complex out-of-equilibrium microstructures, pronounced element segregation and crack formation in the bulk alloy, which are usually the same alloys that are used for conventional manufacturing technologies such as casting [1,2,10]. The successful application of SLM for a wide range of materials requires a better understanding of the material mechanisms during the consolidation step and possibly the development of alloys that are better suitable for the SLM process. It was shown by some of the present authors that the systematic study of the phase and microstructure formation upon RS in Ti-Al and Ti-Al-Nb alloys is useful to understand e.g. changed solidification paths in comparison with low cooling rates and finally to develop an Ti-Al-Nb alloy that showed a better SLM processability than conventional alloys [11–14]. It is therefore assumed that a similar approach may help optimize Cu-Sn(-Ti) alloys for SLM.

The solidification behavior of Cu-rich (>70 wt.%) Cu-Sn alloys and the resulting microstructures have been extensively studied by several researchers [3,15–18] for slow cooling conditions as they occurred e.g. during casting or brazing. Fig. 1 shows

the Cu-Sn phase diagram according to the latest assessments by Fürtauer et al. [19] and Li et al. [20]. While the phase morphologies after solidification are strongly influenced by the composition with regard to the peritectic concentration (hypo- or hyperperitectic alloys), the as-cast microstructures usually consist of α-(Cu) and δ [4,17].

Systematic studies concerning the phase and microstructure formation in Cu-Sn alloys at different cooling rates are scarce. By varying the cooling rates between 5 K/min and 50 K/min in Differential Scanning Calorimetry (DSC), Zhai et al. [21] found that even low cooling rates could significantly influence the phase transformation paths of peritectic 22 wt.% Sn alloy. Only few efforts on RS studies of Cu-Sn based alloys were made to understand the correlation between microstructure and cooling history. To figure out the rapid solidified microstructure of hypo-peritectic Cu-Sn alloys for welding joints, Zhai et al. looked into the microstructure of melt-spun Cu-x%Sn (wt.%, x=7, 13.5, 20, hereafter composition is in wt.% if it is not noted otherwise) at high cooling rates in the order of 10^6 K/s [22,23]. Under substantial undercooling condition, Cu-70%Sn droplets prepared by Zhai [24] in the drop tube experienced growth mechanism transition from peritectic transformation to the direct nucleation and growth of peritectic phase at the cooling rate of 10^2 to 10^4 K/s. The addition of a certain amount of Ti into Cu-Sn system resulted in the modification of microstructural morphologies and the formation of a ternary intermetallic phase that completely replaced the binary intermetallic phase as demonstrated by Spierings et al. [8].

The present work is a systematic study of the microstructure and phase formation in Cu-rich Cu-Sn and Cu-Sn-Ti alloys under rapid solidification conditions as a function of the alloy composition and cooling rate. The cooling rates were varied in a range between 10^3-10^4 K/s in order to mimic the conditions during SLM with the reported cooling rates. The experimental setup reported in [11] is utilized to produce specimens that rapidly solidified at various cooling rates by varying the droplet sizes. The aim was to find strategies for optimizing the composition of Cu-Sn and Cu-Sn-Ti alloys for potential use in additive manufacturing or other processes involving rapid solidification.

2 Materials and methods

2.1 Alloy selection and preparation

For this work, five binary Cu-Sn alloys and five ternary Cu-Sn-Ti were prepared and investigated. The selected binary alloy compositions are indicated in the Cu-Sn phase diagram in Fig. 1 which has been calculated using the Thermocalc software package in combination with the latest thermodynamic assessment [19]. As can be seen, three hypo-peritectic alloys, one near-peritectic and one hyper-peritectic alloy are considered. The compositions of the selected Cu-Sn-Ti alloys are indicated in the liquidus projection in Fig. 2a as well as in the vertical sections Cu20Sn-Ti and Cu25Sn-Ti in Fig. 2b and c, which were calculated based on the assessment of Wang et al. [20]. Two alloys on either side of the monovariant line separating the α-(Cu) and $(Cu,Sn)_3Ti_5$ primary solidification phase fields were selected. In addition, the commercial alloy Cu-14.4Sn-10.2Ti-1.5Zr, which had been used as matrix material for producing metal-diamond composites by SLM [8], was selected. The compositions of all alloys are listed in Table 1. Crystallographic information of the equilibrium phases occurring in the compositional range of interest are listed in Table 2 [18,20].

The raw materials used for producing the master alloys were copper shot (99.999%), tin shot (99.99+%) and titanium slug (99.98%) supplied by Alfa-Aesar, Germany. Each alloy had a mass of about 2 g and was prepared in arc furnace filled with 500 mbar Ar protection gas purified by an OXISORB cartridge (Messer). All alloys were molten for 8 times in total and inverted after every second melting to ensure homogeneity. The material losses after arc melting were lower than 0.2%, thus no chemical analysis was carried out. Note that the reference alloy was prepared directly from commercial pre-alloyed powder in arc furnace.
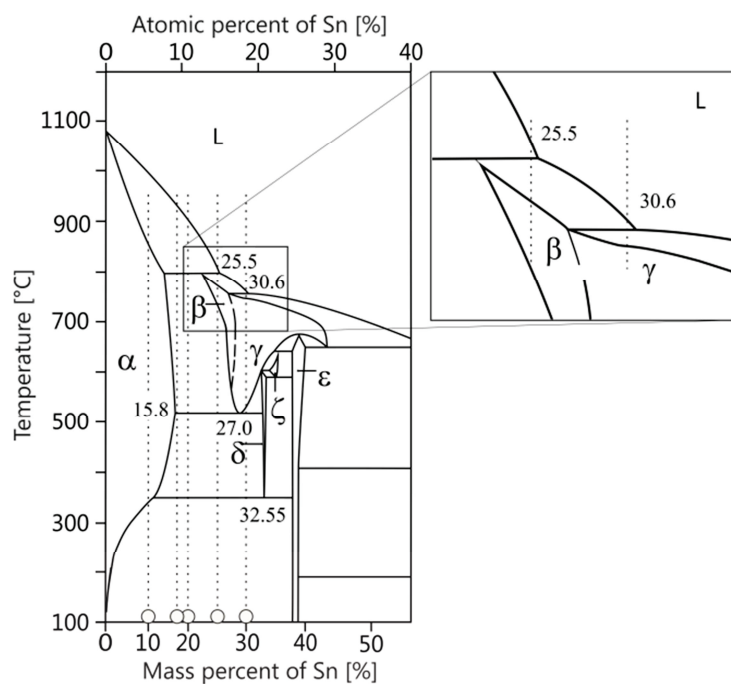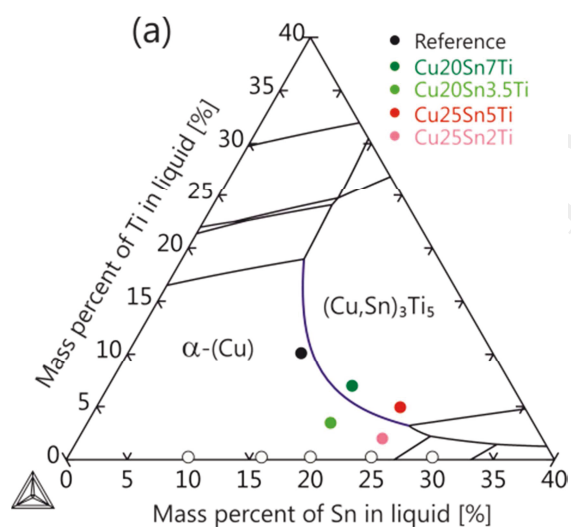
Fig. 1 Phase diagram of binary Cu-Sn using the assessment published in [20]. Five compositions marked by empty circles are 10, 16, 20, 25 and 30Sn, respectively.
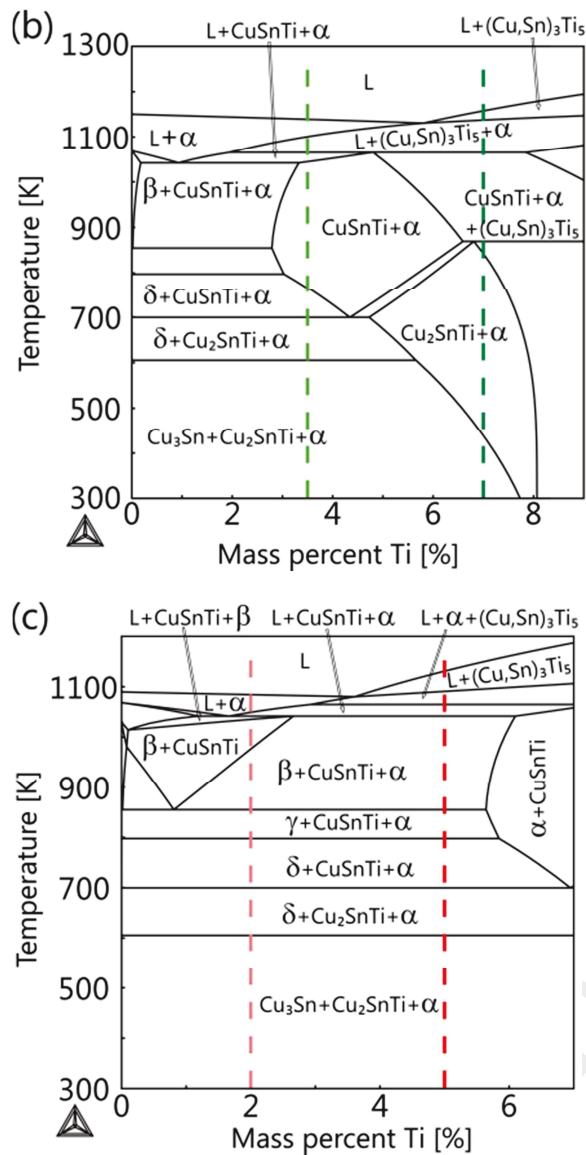
Fig. 2 (a). Calculated liquidus projection of Cu-Sn-Ti ternary system; vertical sections at 20Sn (b) and 25Sn (c). The thermodynamic database from [18] was applied for calculation. To include reference alloy in the liquidus projection, the low amount of Zr in the alloy is neglected.

2.2 Rapid solidification experiments and sample characterization

RS experiments were performed using small samples (4 - 270 mg) that were cut from the respective master alloy samples using the same setup as described in [11]. The melting of the alloys resulted in spheres with three different radii of 0.5, 1 and 2 mm, respectively.

Finite Element Modeling (FEM) was applied to estimate the cooling rates as a function of the specimen diameter using Abaqus/CAE 6.13-2 (3DS Simulia) with a 160,000 hexahedral (DC3D8) element mesh. Detailed descriptions of the model were published in a previous publication [11]. The height to radius ratio was measured as 1.6 for specimens of 2 mm in radius and 1.8 for specimens of 1 and 0.5 mm in radius.

In the current model, the initial droplet temperature was 1400 K and that of the crucible 300 K. Two types of heat transfer were considered, i.e. thermal conduction and surface radiation. The temperature-dependent thermophysical properties of the present two systems such as density, thermal conductivity and specific heat were taken from [25] or were estimated using Thermocalc from room temperature to 200 K above liquidus temperature. Other parameters such as liquidus/solidus temperature and fusion enthalpy were measured by DSC at a heating/cooling rate of 10 K/min. The cooling rate in the center of the sphere at the solidus temperature was considered in this work, and the subsequent structural analyses were also done at the approximately same position. Fig. 3 demonstrates one temperature profile in the Cu10Sn sphere of 1 mm radius as an example. At the solidus temperature of 1119 K of this alloy, a cooling rate of 5000 K/s is calculated. According to the FE simulations, cooling rates between 1300 K/s and 21600 K/s could be achieved with the current setup for Cu-Sn based alloys. The cooling rates at solidus and liquidus temperature were calculated and compared. The difference is small and within the same order of magnitude. Undercooling is required for nucleation and growth of nuclei, which means that the temperature after the passage of the solidification front is between liquidus and solidus temperature. It therefore appears to be reasonable to present the cooling rate rather at the solidus temperature than that at the liquidus temperature.
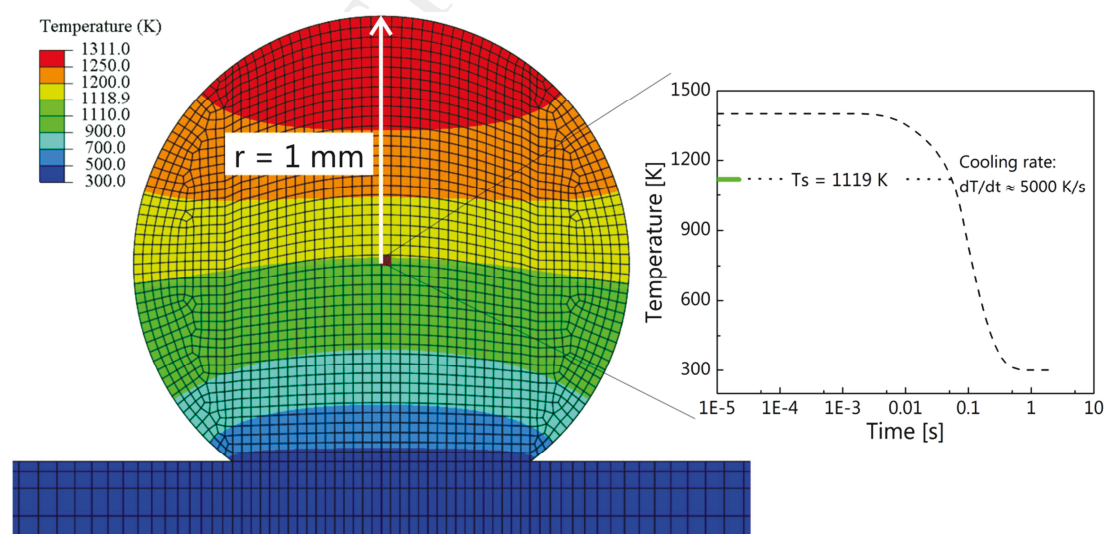

Fig. 3 Temperature gradient map at the cross section of the Cu10Sn sphere of 1 mm in radius during solidification. Based on the temperature history, the cooling rate in the sphere center was calculated at the solidus temperature of Cu10Sn.

DSC tests were carried out with a Netzsch DSC 404C apparatus. Small pieces (5 - 10 mg) of alloys were placed in the center of Yittria coated alumina crucibles to avoid reaction of reactive Ti in the melt with the crucible. The chamber was evacuated and purged with pure argon gas for three cycles to prevent side reactions of alloys plus oxygen. The DSC thermal analyses were performed at the scan rate of 10 K/min and the maximum temperature was 50 K above the liquidus temperature.

After the RS experiments, all specimens were cold mounted into epoxy resin, ground and polished with 3 μm diamond suspension followed by final polishing with 50 nm silica solution. The polished vertical sections of the spheres were characterized by X-ray diffraction (XRD) as well as with EDX and SEM BSE imaging. XRD was performed using Cu Kα radiation on Bruker D8 DISCOVER equipped with a LynxEye detector. X-rays were produced by a copper-radiation source at an accelerating voltage of 40kV and an electron current of 40 mA. A Ni-filter was utilized for absorption of Cu Kβ emission and the step size was 0.02° (2θ). Pinhole snouts with diameters of 2 mm and 1 mm were used to reduce the beam size onto the small polished sample surfaces to minimize background noise. The deformation-free surfaces were investigated under scanning electron microscope using a FEI NanoSEM 230 equipped with BSE and EDX (EDAX) detectors.

Table 1. Nominal compositions of Cu-Sn and Cu-Sn-Ti alloys studied in this work

Binary alloys	Cu	Sn	Ternary alloys	Cu	Sn	Ti	Zr
Cu10Sn	90	10	Reference alloy	73.9	14.4	10.2	1.5
Cu16Sn	84	16	Cu20Sn3.5Ti	76.5	20	3.5	
Cu20Sn	80	20	Cu20Sn7Ti	73	20	7	
Cu25Sn	75	25	Cu25Sn2Ti	73	25	2	
Cu30Sn	70	30	Cu25Sn5Ti	70	25	5	

Table 2. Crystallographic data of Cu-Sn [20] and Cu-Sn-Ti phases [18] in the compositional range of interest

Phase	Stoichiometry	Type	Pearson symbol	Space group	No.	a (Å)	b (Å)	c (Å)	β (°)
α-(Cu)	(Cu)	Cu	cF4	Fm-3m	225	3.61443	–	–	90
β	$Cu_{17}Sn_3$	W	cI2	Im-3m	229	3.0261	–	–	90
γ	Cu_3Sn	BiF_3	cF16	Fm-3m	225	6.1176	–	–	90
δ	$Cu_{41}Sn_{11}$	$Cu_{41}Sn_{11}$	cF416	F-43m	216	17.98	–	–	90
ε	Cu_3Sn	Cu_3Ti	oC80	Cmcm	63	5.529	47.75	4.323	90

(Cu,Sn)$_3$Ti$_5$	Cu$_{0.52}$Sn$_3$Ti$_5$	Nb$_{10}$Ge$_7$	hP17	Pmcm	193	8.151	–	5.590	90
CuSnTi	TiCuSn	LiGaGe	hP6	Pmc	186	4.3972	–	6.0168	90
Cu$_2$SnTi	Cu(Sn.5Ti.5)	CsCl	cP2	Pm-3m	221	2.960	–	–	90

3 Results and discussion

3.1 Binary Cu-Sn alloys

Fig. 4 illustrates the microstructure of Cu25Sn after melting and solidification in the DSC furnace consisting of primary α and lamellar α + δ (as confirmed by XRD) formed via eutectoid reaction (Y → α + δ). All binary alloys exhibited a eutectoid microstructure like the one of Cu25Sn, and a peak at 521 °C was observed in the DSC signal indicating the eutectoid reaction. Since the same phase constituents but different phase fractions were observed in RS of Cu10Sn, Cu16Sn and Cu20Sn, only an image of RS of Cu20Sn is representatively displayed in Fig. 5a. The SEM micrographs were taken at the center of the spheres for which the cooling rates have been computed. The microstructures of rapidly consolidated Cu25Sn and Cu30Sn depicted in Fig. 5b and c are different from those of the alloys with a lower nominal Sn content. It is evident that all alloys show a two-phase microstructure except Cu25Sn which has a single phase microstructure with coarse grains. The contrast in the BSE micrograph of Cu25Sn (Fig. 5b) is attributed to grain orientation differences. The point EDX measurement results reveal that in Cu20Sn ~10% Sn is dissolved in α-(Cu) but ~25% Sn in the second phase. A homogeneous Sn concentration of ~25% was detected in Cu25Sn; in Cu30Sn, an additional phase with a different composition (~33%) was observed (cf. Fig. 5c).

The peaks corresponding to α-(Cu) as shown in Fig. 6 are found in alloys with less than 20% Sn, whereas peaks corresponding to the δ-phase are observed in Cu30Sn. Numerous other intensive peaks could not be assigned any of the equilibrium phases shown in the phase diagram in Fig. 1. The occurrence of a metastable Cu$_{5.6}$Sn phase with simple tetragonal crystal structure (a = b = 0.985 nm, c = 1.1028 nm) was reported in rapidly solidified peritectic Cu-Sn alloys produced by melt-spinning in [22] and plated films in [26]. Our analysis of the XRD spectra and comparison with the literature data [26] leads therefore to the conclusion that the unknown peaks can be attributed to the Cu$_{5.6}$Sn phase.
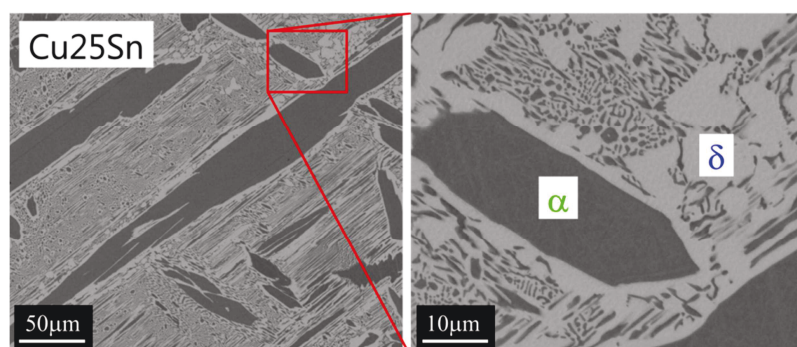
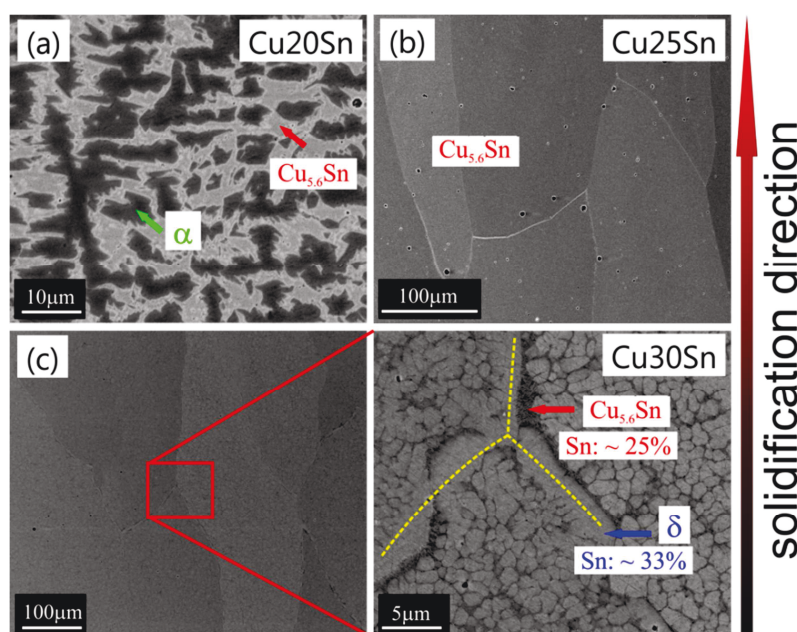**Fig. 4** Microstructure of Cu25Sn which solidified at the cooling rate of 10 K/min

Fig. 5 BSE images of the rapid solidified microstructures of Cu20Sn (a), Cu25Sn (b) and Cu30Sn (c) of 2 mm in radius. Porosity from RS can be present, e.g. in Cu25Sn (b).
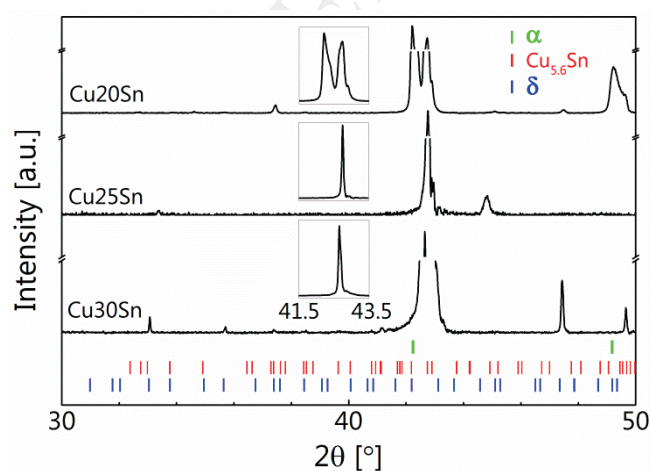

Fig. 6 XRD patterns of Cu20Sn, Cu25Sn, Cu30Sn alloys. The three inserts are the initial strongest peaks of each alloy between 41.5° and 43.5°.

In Fig. 7, the Cooling rate-Composition–Phase (CCP) map which summarizes the effect of cooling rates and Sn content on RS microstructure in terms of phase constituents for cooling rates 10^3 K/s < dT/dt < 2×10^4 K/s is shown. The microstructures observed after slow cooling in the DSC furnace are shown for comparison. With increasing Sn content, the cooling rate of specimens with the same diameter decreases due to the decrease of the thermal conductivity with increasing solute concentration. As implicated in the phase diagram, all selected binary alloys which cool down at 10 K/min consist of α and δ phases. An increase of cooling rates results in the presence of the metastable $Cu_{5.6}Sn$ phase. Scudino et al. [4] observed the α and δ phase in SLM fabricated samples as well as in cast Cu10Sn bronze. However, the compositions of the observed phases were not reported. A possible explanation for this effect might be that the $Cu_{5.6}Sn$ phase was transformed into δ due to the multiple heat treatments resulting from the layerwise heating and cooling during SLM process. Zhai et al. [24] proposed that this metastable phase formed via martensitic transformation during fast cooling and that the morphology of $Cu_{5.6}Sn$ phase remained from the parent β phase.

Considering the equilibrium phase diagram presented in Fig. 1, the α-(Cu) phase is expected as the primary solidification phase for all alloys with a Sn amount <25.5% and β phase for the Cu30Sn alloy. The experimental findings as described above also suggest primary α-(Cu) solidification in the alloys Cu10Sn, Cu16Sn and Cu20Sn. However, the coarse and elongated grains observed in Cu25Sn (cf. Fig. 5b) indicate that the high temperature β phase supersaturated with Sn forms during solidification. Similar for the Cu30Sn alloy (cf. Fig. 5c), coarse Y grains form during RS. The yellow lines indicate the grain boundaries of the parent Y phase. Since these two alloys pass the L+ α-(Cu) and L+ β only in a very narrow temperature range upon cooling, it is possible that the formation of primary α-(Cu) in Cu25Sn and β in Cu30Sn is suppressed due to the short time for nucleation and growth and the constrained diffusion, and β and Y, respectively, are formed instead. The following eutectoid reaction is also suppressed in Cu25Sn alloy due to the low mobility of large Sn atoms in the solid phase, i.e. that the parent β phase with the same composition as the melt directly crystallizes from the melt.

While under equilibrium conditions, the energy is minimized by the formation of two phases with different compositions, diffusion can be strongly reduced during rapid cooling, which hinders the formation of the equilibrium phases. As shown in a

previous work [11], the phase formation sequence in alloys during RS can be interpreted using so-called phase selection hierarchy maps based on the T_0 temperature, i.e. the temperature at which the Gibbs free energies of two phases with the same composition are equal. Considering for example L and α-(Cu) in Cu20Sn, the formation of α-(Cu) dissolved with 20% Sn is expected as soon as $T < T_{0,L\rightarrow\alpha\text{-(Cu)}}$, where $G_{\alpha\text{-(Cu)}} < G_L$. The energy of the intersection point of the Gibbs free energy curves where $G_L = G_{\alpha\text{-(Cu)}}$ is always larger than the energy of the points lying on the common tangent line; the α-(Cu) phase is thus supersaturated above its equilibrium limit of solubility. Likewise, $T_{0,L\rightarrow\beta}$ and $T_{0,L\rightarrow\gamma}$ can be calculated. In the absence of partitioning, i.e. when diffusion is completely suppressed, the transformation with the highest T_0 is the most likely one to occur. Fig. 8 shows the calculated T_0 temperatures for the phase transformations L→α-(Cu), L→β and L→Y in the composition range of interest. The presence of α-(Cu) as primary phase in the Cu20Sn alloys after RS suggests that the nucleation and growth of α-(Cu) phase are still preferred over that of the β phase, i.e. that partitioning still occurs. The T_0 curve for the transformation L→β intersects the one for L→α-(Cu) at 17.9% Sn and the one for L→Y at 26.2% Sn. The formation of primary β in the Cu25Sn alloy and Y in the Cu30Sn alloy may thus be also explained by the thermodynamic preference of these two phases upon RS as shown in Fig. 8. In the Cu30Sn alloy, primary Y phase undergoes a solid-state transformation into Sn depleted and enriched phases as shown in Fig. 5c. Since the high temperature Y phase is unstable at ambient temperature [19], ordering of Sn atoms over short distances occurs in Sn enriched region to form dendritic δ phase while $Cu_{5.6}Sn$ forms in the Sn depleted region via martensitic transformation. The δ phase has the superstructure with F symmetry of Y-brasses (cf. Table 2) where close contact between larger Sn atoms are prevented [27]. This mechanism of dendritic growth in the solid-state phase transformation was observed in Cu-31.3 wt.% Sn and other binary systems [28] and is attributed to the fast bulk diffusion and small lattice parameter mismatch. As grain boundaries are fast diffusion passages, the grains of $Cu_{5.6}Sn$ and δ phase at the parent grain boundaries of Cu30Sn are larger than the grains within the parent grain (cf. Fig. 5c).
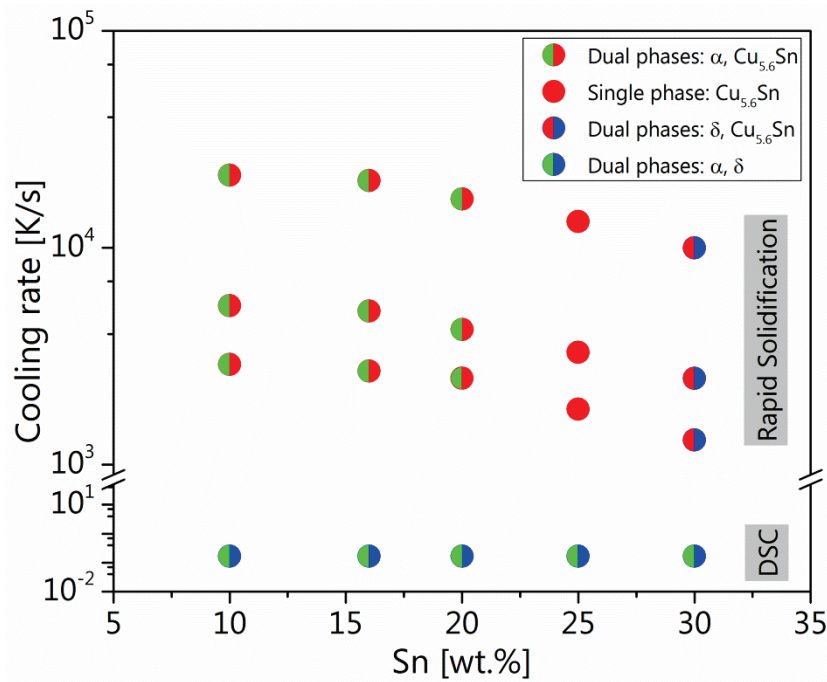
Fig. 7 Cooling rate-Composition-Phase map of binary Cu-Sn alloys. Green, red and blue color represents α, $Cu_{5.65}Sn$ and δ phase, respectively.
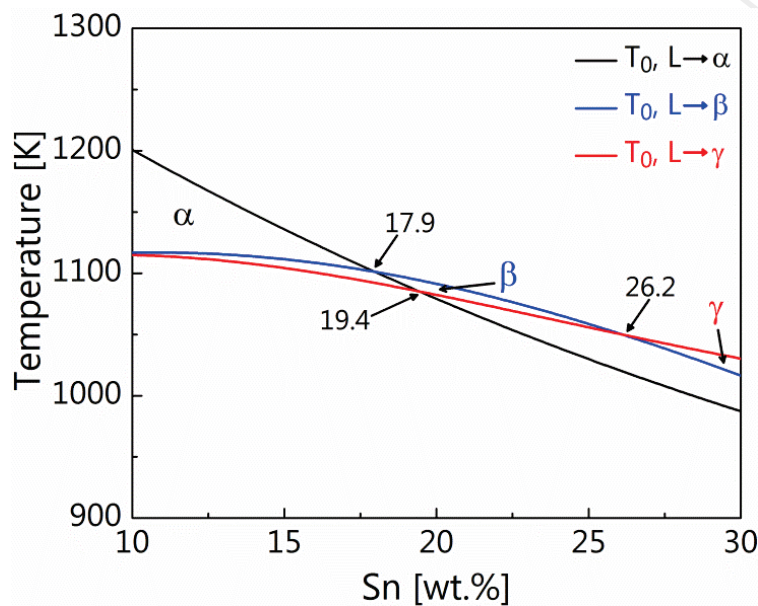

Fig. 8 Map of thermodynamic phase selection hierarchy as a function of temperature and Sn content. The solid lines are the T_0 curves for the solidification of α, β and Y, respectively.

3.2 Ternary Cu-Sn-Ti alloys

Fig. 9 shows the microstructure of the Cu-14.4Sn-10.2Ti-1.5Zr reference alloy at four different cooling rates. At low cooling rate (10 K/min), coarse equiaxed α-(Cu) grains and facetted $(Cu,Sn)_3Ti_5$ grains are observed (cf. Fig. 9a). At the cooling rate of 2300 K/s, primary α dendrites due to constitutional undercooling and fine lamellar structure inherited from eutectic reaction remain in the rapidly solidified microstructure as presented in Fig. 9b. With a further increase of the cooling rate up to 5000 K/s,

a similar microstructure is observed. In addition, a dark colored phase that was apparently frozen during its growth is visible in Fig. 9c. At a cooling rate of $2*10^4$ K/s, the originally fine dendrites of the dark phase are fully embedded in the eutectic lamellar structure. It can be concluded that the dendritic primary α-(Cu) becomes less favored and can even be completely suppressed by increasing cooling rates. Evidently, the lamellar spacing decreases with increasing cooling rate.

As illustrated in the XRD spectra from Fig. 12, peaks corresponding to α-(Cu) as well as to the intermetallic $(Cu,Sn)_3Ti_5$ phase can be observed in all samples. In addition, peaks corresponding to the $Cu_{5.6}Sn$ phase are also present in most alloys except for the reference alloy that only consists of $(Cu,Sn)_3Ti_5$ and α-(Cu). Since only two phases were identified from XRD measurements, it is most likely that the Ti enriched dark phase shown in Fig. 9c is $(Cu,Sn)_3Ti_5$. It has been reported in [16] that $(Cu,Sn)_3Ti_5$ have a large solubility range for Cu and Sn. This suggests that at high cooling rate the nucleation of $(Cu,Sn)_3Ti_5$ is rapid enough to supersede the nucleation and growth of dendritic α-(Cu) crystals. From the reference alloy to other alloys, the peak positions of α-(Cu) shift towards lower-angles. An evident explanation is that a higher concentration of solute atoms (~9 at.%) in α-(Cu) phase in other alloys was measured than that (~2 at.% Sn and ~4 at.% Ti) in dendritic α-(Cu) grains from point EDX, which leads to an increase of the lattice constant.

Fig. 10 shows representative microstructures from the center of ternary specimens with a radius of 2 mm. The smaller spheres have the rather similar microstructure but smaller grain sizes. Grain refinement is achieved by increasing the nucleation rate depending on the undercooling of the melt. To analyze the fine lamellar grain structure, qualitative EDX mapping (cf. Fig. 11) was conducted on a Cu20Sn7Ti alloy, giving information on the X-ray intensity distributions from Ti, Cu and Sn elements. A higher Sn concentration in the metastable $Cu_{5.6}Sn$ phase than that in α-(Cu) gives rise to the contrast in the BSE micrographs. In comparison with α-(Cu) and $Cu_{5.6}Sn$, $(Cu,Sn)_3Ti_5$ is characterized by Cu depletion but an increased amount of Ti and Sn. Similar to the large $(Cu,Sn)_3Ti_5$ facets confirmed by point EDX, large amounts of Ti but comparable amount of Cu are dissolved in the fine lamellae. Considering the XRD results where only $(Cu,Sn)_3Ti_5$, α and $Cu_{5.6}Sn$ phases are identified, it can be assumed that the fine lamellar structures are also the $(Cu,Sn)_3Ti_5$ phase. The morphology of the $(Cu,Sn)_3Ti_5$ phase is either facetted as the primary phase from melt or lamellar due to the monovariant eutectic reaction (L → α + $(Cu,Sn)_3Ti_5$). Although $(Cu,Sn)_3Ti_5$ is thermodynami-

cally not favored at ambient temperature, it did not transform into other intermetallic phases as indicated in the phase diagram (Fig. 2b and c) due to the constrained diffusion process during rapid cooling.

Table 3 summarizes the phases observed in RS Cu-Sn and Cu-Sn-Ti alloys (cf. Fig. 5 and

Fig. 10). For Cu20SnxTi (x=0, 3.5, 7) alloys, the addition of Ti promotes the formation of lamellar $(Cu,Sn)_3Ti_5$ while at a higher amount of Ti primary $(Cu,Sn)_3Ti_5$ rather than α-(Cu) is present. Since only a negligible amount of Ti can be dissolved in the α-(Cu) [18], most of Ti segregates from dendritic α into the melt, resulting in the formation of $(Cu,Sn)_3Ti_5$ at the solidification front. For Cu25SnxTi (x=0, 2, 5) alloys, only 2% Ti changes the entire microstructure from coarse grains of single $Cu_{5.6}Sn$ phase to small grains of $Cu_{5.6}Sn$ surrounded by lamellae. From both sets of alloys, an increasing amount of Ti promotes the formation of $(Cu,Sn)_3Ti_5$ and α-(Cu) phase but impairs $Cu_{5.6}Sn$ phase. Obviously, other ternary compounds expected from phase diagrams do not form, most likely due to the restricted diffusion of solutes in the solid $(Cu,Sn)_3Ti_5$ phase. $(Cu,Sn)_3Ti_5$ is stabilized by rapid cooling as well as slow cooling as shown in Fig. 9a.
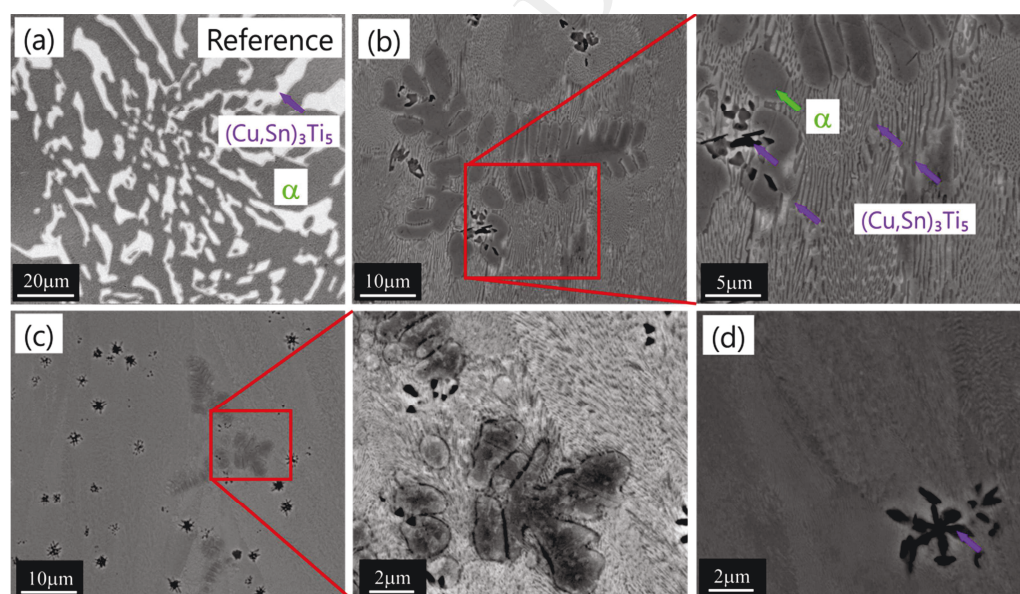

Fig. 9 The microstructural micrographs of reference alloy that solidified at cooling rates of 10 K/min (a), 2300 K/s (b), 5000 K/s (c) and 20000 K/s (d)
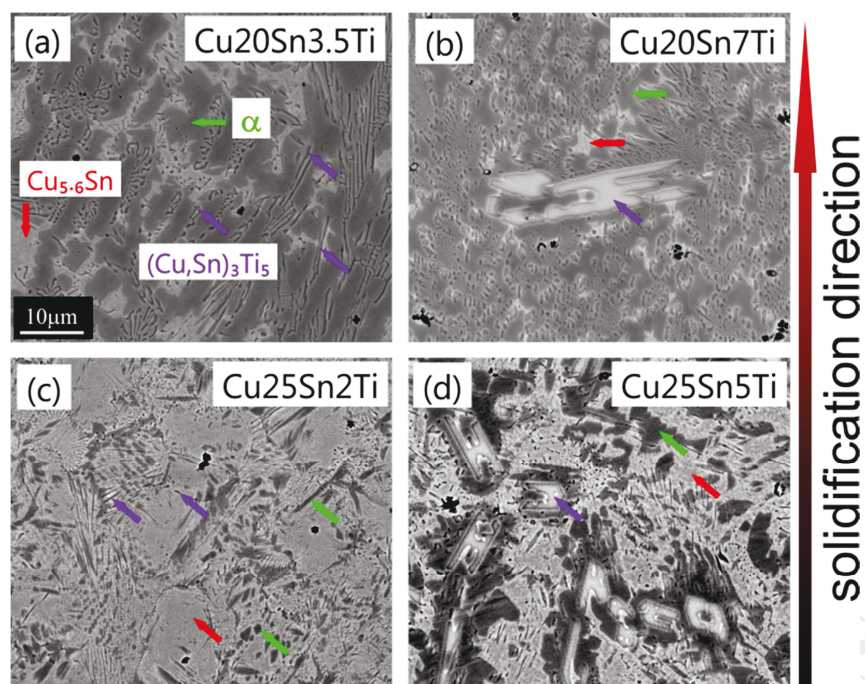
Fig. 10 BSE images of largest spheres (r = 2 mm). Specimens of smaller sizes have the same phase constituents and similar microstructural morphology with the illustrated microstructures. Arrows with the same color represent the same phase.
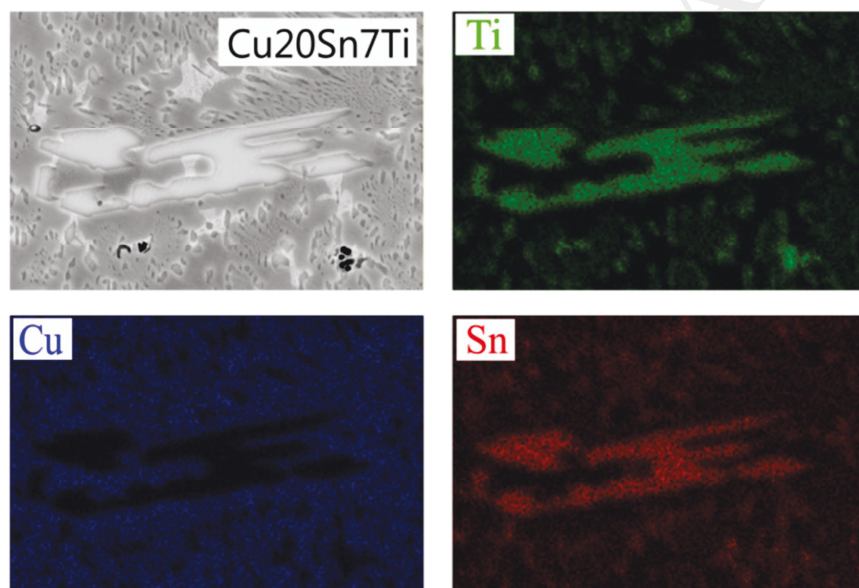

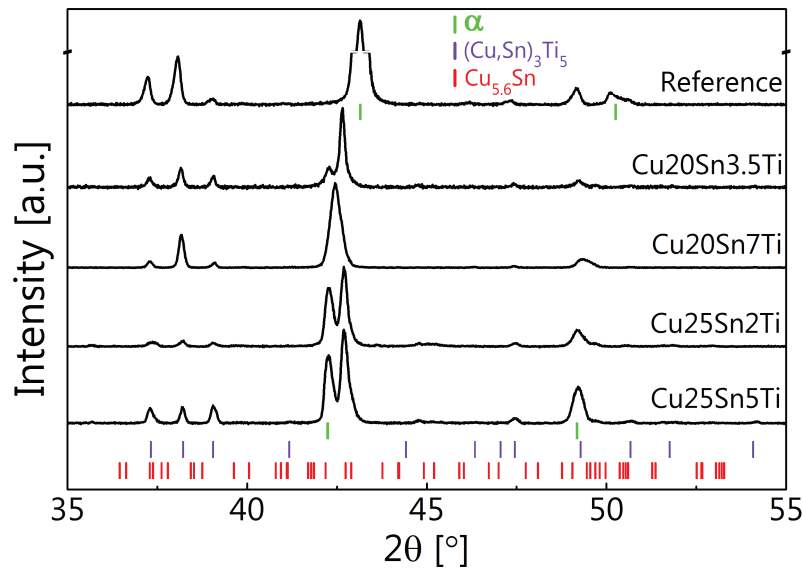**Fig. 11** Elemental maps for Ti, Cu and Sn of a region containing primary $(Cu,Sn)_3Ti_5$

Fig. 12 Representative XRD curves of largest spheres for phase identification

Table 3. Summary of phases observed in the RS Cu-Sn and Cu-Sn-Ti specimens

Cu-Sn and Cu-Sn-Ti alloys	Primary phase			Other phases		
Radius [mm]	2	1	0.5	2	1	0.5
Reference alloy	α		$(Cu,Sn)_3Ti_5$	$(Cu,Sn)_3Ti_5$		α
Cu20Sn	α			β $(Cu_{5.6}Sn)$		
Cu20Sn3.5Ti	α			$(Cu,Sn)_3Ti_5$, β $(Cu_{5.6}Sn)$		
Cu20Sn7Ti	$(Cu,Sn)_3Ti_5$			α, β $(Cu_{5.6}Sn)$		
Cu25Sn	β $(Cu_{5.6}Sn)$			-		
Cu25Sn2Ti	β $(Cu_{5.6}Sn)$			α, $(Cu,Sn)_3Ti_5$		
Cu25Sn5Ti	$(Cu,Sn)_3Ti_5$			α, β $(Cu_{5.6}Sn)$		

Note: (1). 2, 1 and 0.5 are the radii of RS specimens in correspondence with the increase of cooling rates. (2). Primary β does not exist in the final microstructures because it transforms into $Cu_{5.6}Sn$.

4. Conclusions

The present rapid solidification studies give insight into the influence of cooling rates and compositions on the out-of-equilibrium microstructure formation of Cu-Sn and Cu-Sn-Ti alloys including phase constituents and morphologies.

In the Cu-Sn binary system, the metastable $Cu_{5.6}Sn$ phase is transformed from a high temperature phase in the compositional range of interest. At RS conditions, primary α dendrites and metastable $Cu_{5.6}Sn$ compose the microstructure of Cu-xSn (x=10, 16, 20); coarse columnar grains of single $Cu_{5.6}Sn$ phase are in the microstructure of Cu25Sn alloy; in Cu30Sn alloy, coarse parent grains are transformed into Sn enriched δ phase and Sn depleted $Cu_{5.6}Sn$ phase. Furthermore, β and Y are selected as primary phases in the 25% Sn and 30% Sn alloy, respectively. Those phases are

thermodynamically preferred in the partitionless solidification at each composition. In addition, different microstructural morphologies varying from primary α dendrites to coarse columnar β/Υ grains develop with increasing Sn content.

In all Cu-Sn-Ti ternary alloys, $(Cu,Sn)_3Ti_5$ forms without decomposition into other ternary compounds since the rapid cooling hinders diffusion of solutes in solid. Depending on the formation mechanisms, $(Cu,Sn)_3Ti_5$ is either facetted as primary phase or lamellar due to a mono-variant eutectic reaction. Additionally, the increase of Ti content increases the fraction of $(Cu,Sn)_3Ti_5$ and α phases but decreases the amount of $Cu_{5.6}Sn$ phase due to the fact that a negligible amount of Ti can be dissolved in the α phase. The cooling rates mainly influence the phase formation of Cu-Sn binary system.

Acknowledgements

References

[1]   D. Herzog, V. Seyda, E. Wycisk, C. Emmelmann, Additive manufacturing of metals, Acta Mater. 117 (2016) 371–392. doi:10.1016/j.actamat.2016.07.019.

[2]   D.D. Gu, W. Meiners, K. Wissenbach, R. Poprawe, Laser additive manufacturing of metallic components: materials, processes and mechanisms, Int. Mater. Rev. 57 (2012) 133–164. doi:10.1179/1743280411Y.0000000014.

[3]   F. Kohler, T. Campanella, S. Nakanishi, M. Rappaz, Application of single pan thermal analysis to Cu–Sn peritectic alloys, Acta Mater. 56 (2008) 1519–1528. doi:10.1016/j.actamat.2007.12.006.

[4]   S. Scudino, C. Unterdörfer, K.G. Prashanth, H. Attar, N. Ellendt, V. Uhlenwinkel, J. Eckert, Additive manufacturing of Cu–10Sn bronze, Mater. Lett. 156 (2015) 202–204. doi:10.1016/j.matlet.2015.05.076.

[5]   Y.-C. Bai, Y.-Q. Yang, D. Wang, A.-M. Wang, High relative density tin bronze parts directly manufactured by selective laser melting, Guangxue Jingmi GongchengOptics Precis. Eng. 24 (2016) 484–492. doi:10.3788/OPE.20162413.0484.

[6]   A.P. Ventura, C.A. Wade, G. Pawlikowski, M. Bayes, M. Watanabe, W.Z. Misiolek, Mechanical Properties and Microstructural Characterization of Cu-4.3 Pct Sn Fabricated by Selective Laser Melting, Metall. Mater. Trans. A. 48 (2017) 178–187. doi:10.1007/s11661-016-3779-x.

[7]   M. Iravani, A. Khajepour, S. Corbin, S. Esmaeili, Pre-placed laser cladding of metal matrix diamond composite on mild steel, Surf. Coat. Technol. 206 (2012) 2089–2097. doi:10.1016/j.surfcoat.2011.09.027.

[8]   A.B. Spierings, C. Leinenbach, C. Kenel, K. Wegener, Processing of metal-diamond-composites us-
      ing selective laser melting, Rapid Prototyp. J. 21 (2015) 130–136. doi:10.1108/RPJ-11-2014-0156.

[9]   J. Suryawanshi, K.G. Prashanth, S. Scudino, J. Eckert, O. Prakash, U. Ramamurty, Simultaneous en-
      hancements of strength and toughness in an Al-12Si alloy synthesized using selective laser melt-
      ing, Acta Mater. 115 (2016) 285–294. doi:10.1016/j.actamat.2016.06.009.

[10] E.O. Olakanmi, R.F. Cochrane, K.W. Dalgarno, A review on selective laser sintering/melting
      (SLS/SLM) of aluminium alloy powders: Processing, microstructure, and properties, Prog. Mater.
      Sci. 74 (2015) 401–477.

[11] C. Kenel, C. Leinenbach, Influence of cooling rate on microstructure formation during rapid so-
      lidification of binary TiAl alloys, J. Alloys Compd. 637 (2015) 242–247.
      doi:10.1016/j.jallcom.2015.03.016.

[12] C. Kenel, C. Leinenbach, Influence of Nb and Mo on microstructure formation of rapidly solidified
      ternary Ti–Al-(Nb, Mo) alloys, Intermetallics. 69 (2016) 82–89. doi:10.1016/j.intermet.2015.10.018.

[13] C. Kenel, D. Grolimund, J.L. Fife, V.A. Samson, S. Van Petegem, H. Van Swygenhoven, C. Leinen-
      bach, Combined in situ synchrotron micro X-ray diffraction and high-speed imaging on rapidly
      heated and solidified Ti–48Al under additive manufacturing conditions, Scr. Mater. 114 (2016)
      117–120. doi:10.1016/j.scriptamat.2015.12.009.

[14] C. Kenel, K. Dawson, J. Barras, C. Hauser, G. Dasargyri, T. Bauer, A. Colella, A.B. Spierings, G.J. Tat-
      lock, C. Leinenbach, K. Wegener, Microstructure and oxide particle stability in a novel ODS γ-TiAl
      alloy processed by spark plasma sintering and laser additive manufacturing, Intermetallics. 90
      (2017) 63–73. doi:10.1016/j.intermet.2017.07.004.

[15] F. Kohler, L. Germond, J.-D. Wagnière, M. Rappaz, Peritectic solidification of Cu–Sn alloys: Micro-
      structural competition at low speed, Acta Mater. 57 (2009) 56–68.
      doi:10.1016/j.actamat.2008.08.058.

[16] M. Rappaz, F. Kohler, J. Valloton, A.B. Phillion, M. Stampanoni, Connectivity of Phases and Growth
      Mechanisms in Peritectic Alloys Solidified at Low Speed: an X-Ray Tomography Study of Cu-Sn,
      Metall. Mater. Trans. A. 41 (2010) 563–567. doi:10.1007/s11661-009-0118-5.

[17] J. Valloton, J.-D. Wagnière, M. Rappaz, Competition of the primary and peritectic phases in hy-
      poperitectic Cu–Sn alloys solidified at low speed in a diffusive regime, Acta Mater. 60 (2012)
      3840–3848. doi:10.1016/j.actamat.2012.03.030.

[18] J. Wang, C. Liu, C. Leinenbach, U.E. Klotz, P.J. Uggowitzer, J.F. Löffler, Experimental investigation
      and thermodynamic assessment of the Cu–Sn–Ti ternary system, Calphad. 35 (2011) 82–94.
      doi:10.1016/j.calphad.2010.12.006.

[19] S. Fürtauer, D. Li, D. Cupid, H. Flandorfer, The Cu–Sn phase diagram, Part I: New experimental re-
      sults, Intermetallics. 34 (2013) 142–147. doi:10.1016/j.intermet.2012.10.004.

[20] D. Li, P. Franke, S. Fürtauer, D. Cupid, H. Flandorfer, The Cu–Sn phase diagram part II: New ther-
      modynamic assessment, Intermetallics. 34 (2013) 148–158. doi:10.1016/j.intermet.2012.10.010.

[21] W. Zhai, W.L. Wang, D.L. Geng, B. Wei, A DSC analysis of thermodynamic properties and solidifi-
      cation characteristics for binary Cu–Sn alloys, Acta Mater. 60 (2012) 6518–6527.
      doi:10.1016/j.actamat.2012.08.013.

[22] Q. Zhai, Y. Yang, J. Xu, X. Guo, Microstructural morphology and phase structure of rapidly solidi-
      fied Cu-Sn alloy, Chin. J. Nonferrous Met. 16 (2006). http://en.cnki.com.cn/Article_en/CJFDTOTAL-
      ZYXZ200608010.htm (accessed March 27, 2017).

[23] Y. Yang, J. Xu, Q. Zhai, Rapid dendritic growth in melt-spun Cu-Sn alloys, Chin. J. Nonferrous Met.
      17 (2007) 1521.

[24] W. Zhai, B. Wei, Direct nucleation and growth of peritectic phase induced by substantial under-
      cooling condition, Mater. Lett. 108 (2013) 145–148. doi:10.1016/j.matlet.2013.06.084.

[25] J. Miettinen, Thermodynamic–kinetic model for the simulation of solidification in binary copper alloys and calculation of thermophysical properties, Comput. Mater. Sci. 36 (2006) 367–380. doi:10.1016/j.commatsci.2005.05.004.

[26] T. Watanabe, Chapter 7 - Database for the Microstructure of Plated Films, in: Nano Plat. - Microstruct. Form. Theory Plated Films Database Plated Films, Elsevier, Oxford, 2004: pp. 255–696. doi:10.1016/B978-008044375-1/50016-6.

[27] M.H. Booth, J.K. Brandon, R.Y. Brizard, C. Chieh, W.B. Pearson, γ-Brasses with F cells, Acta Crystallogr. Sect. B. 33 (1977) 30–36. doi:10.1107/S0567740877002556.

[28] S.W. Husain, M.S. Ahmed, I. Qamar, Dendritic morphology observed in the solid-state precipitation in binary alloys, Metall. Mater. Trans. A. 30 (1999) 1529–1534. doi:10.1007/s11661-999-0089-6.

- Rapid solidification microstructures were studied in Cu-Sn(-Ti) alloys
- Rapid cooling facilitates the formation of metastable $Cu_{5.6}Sn$
- Addition of Ti promotes the formation of $(Cu,Sn)_3Ti_5$
- The microstructural morphology can be tuned by alteration of Ti amount
- High cooling rates deteriorate the formation of primary dendritic α phase